Columnar Joints Produced by Cooling in Basalt

Phillips, J.C.[1*], Humphreys, M.C.S.[2†], Daniels, K.A.[1], Brown, R.J.[3‡] & Witham, F.[1§]

[1] Department of Earth Sciences, University of Bristol, Queens' Road, Bristol, BS8 1RJ, UK

[2] Department of Earth Sciences, University of Cambridge, Downing Street, Cambridge, CB2 3EQ, UK

[3] Department of Earth and Environmental Sciences, The Open University, Walton Hall, Milton Keynes, MK7 6AA, UK

Current addresses:

[†] Department of Earth Sciences, University of Oxford, South Parks Road, Oxford, OX1 3AN, UK

[‡] Department of Earth Sciences, Durham University, Science Labs, Durham, DH1 3LE, UK

[§] Rolls-Royce, Gypsy Patch Lane, Bristol, BS34 7QE, UK

Corresponding Author: j.c.phillips@bristol.ac.uk, phone +441179545241, fax +441179253385

ABSTRACT

Columnar jointing in basaltic lava flows on the island of Staffa, NW Scotland, was studied using a combination of field mapping and measurement of column dimensions, sample petrology and measurements of plagioclase crystal size distributions (CSDs) interpreted using theoretical models of cooling. Four different lava flow units were measured, and column ordering was assessed using the hexagonality index and relative standard deviations of column side length, top

area and internal angle. Upper and lower colonnades consist of dominantly 5, 6 and 7-sided columns, with a hexagonality index value very similar to that of Giant's Causeway and other basaltic columnar jointed localities. CSDs from samples at different heights within one colonnade were used to infer the propagation of the solidus isotherm, which was consistent with a convective cooling mechanism within the colonnade interior. Sample petrology and CSD measurements suggest that entablature can form both by the interaction of propagating joint sets and flooding of the flow surface by water, and the most widely exposed unit on Staffa shows evidence of both mechanisms operating on the same flow. Crystal size distribution measurements can provide a useful tool for field interpretation of lava flow cooling mechanisms.

KEYWORDS

Columnar jointing, lava flow, basalt, crystal size distribution, convective cooling, fracture pattern

1. INTRODUCTION

Polygonal or columnar jointing is found in lava flows with a range of composition from basalt to rhyolite and formed in a range of environments from subaerial to subglacial, and also in some welded pyroclastic deposits. Many dykes and sills are also columnar-jointed. Similar features are also observed in a wide range of materials including muddy sediments (e.g. Weinberger 1999), permafrost (Lachenbruch 1962) and starch-water mixtures (e.g. Müller 1998a; 1998b). Columnar jointed basalts typically show two jointing facies (Fig. 1): a 'colonnade' comprising

48 regular columns with near-planar sides, and an ‘entablature’ with typically thinner, less regular
49 columns that commonly have curving sides (e.g. Tomkeieff 1940; Spry 1962). Some flows also
50 have an upper colonnade section (Fig. 1b); if present, this is typically of a similar thickness or
51 slightly thinner than the lower colonnade (Long and Wood 1986). The presence of the
52 entablature in the absence of an upper colonnade has been explained by increased rates of
53 cooling caused by flooding of the lava surface, allowing water to access the interior of the flow
54 (Saemundsson 1970). This was based on the fine grain-size, skeletal crystal textures and
55 increased amount of mesostasis (fine-grained groundmass material) in entablature samples
56 compared with those from the colonnade, and was supported by the fact that such lavas were
57 emplaced into palaeo-topographic lows, including river valleys (Swanson 1967; Saemundsson
58 1970). An alternative to this interpretation, valid for flows with both upper and lower
59 colonnades, is that the entablature represents the region where the two opposing joint sets meet,
60 resulting in a complicated distribution of stress and hence irregular and curving columns (e.g. Xu
61 1980, reported in Budkewitsch and Robin 1994; Spry 1962). Furthermore, the isotherm velocity
62 (the rate of propagation of a cooling front at a particular temperature) in the centre of a flow is
63 more rapid than at the margins (e.g. Tomkeieff 1940, Grossenbacher and McDuffie 1995), which
64 could result in smaller column diameters. Most recently, Goehring and Morris (2005) observed a
65 discontinuous transition in the scale of jointing in starch-water columnar structures produced at a
66 constant drying rate, and suggested that entablature could form through a similar inherent
67 instability of the system. However, their analogue system differs from cooling lava flows in that
68 joints can only form from the upper surface.
69
70 *Figure 1 here*

71

72 Several previous studies have modelled the thermo-mechanical process of joint formation (e.g.
73 Reiter 1987; Degraff and Aydin 1993; Budkewitsch and Robin 1994; Goehring and Morris
74 2008). Columnar joints are thought to form by spatially-uniform volume contraction during
75 cooling. Stress due to thermal contraction is able to accumulate once the temperature falls below
76 that of elastic behaviour (effectively the glass transition temperature, *Tg,* for typical lava cooling
77 rates), and jointing occurs when the stress exceeds the tensile strength of the material
78 (Budkewitsch and Robin 1994). Thus in a planar layer cooling from above, jointing will
79 propagate progressively downward in increments that roughly follow the passage of the isotherm
80 that defines *Tg*. These joint increments can be observed as *striae* or 'chisel marks' in natural
81 examples of columnar jointed basalt (Fig. 1; Tomkeieff 1940; Ryan and Sammis 1981; Degraff
82 and Aydin 1987). The striae spacing, and thus column diameter, therefore reflect the thermal
83 gradient and cooling rate of the basalt and can be expected to vary with height in a cooling lava
84 flow, dependent on its thermal conditions (e.g. Tomkeieff 1940; Degraff and Aydin 1993;
85 Grossenbacher and McDuffie 1995; Goehring and Morris 2008). Recent field observations and
86 theoretical analysis have shown that constant striae spacing (spacing invariant with height on a
87 given column), as observed at a number of different field localities, is consistent with constant
88 cooling rate controlled by the presence of water inside cooling cracks (Goehring and Morris
89 2008).
90

91 The aim of this study is to investigate in detail the role of the cooling mechanism on columnar
92 jointing patterns, with particular focus on obtaining the best possible constraints from field
93 observations. To do this we conducted a thorough and detailed geological investigation of

94 columnar jointing on the island of Staffa, northwest Scotland, including using field mapping to
95 formally identify different lava flow units, measuring column properties and using petrological
96 methods to estimate emplacement temperatures and cooling rates. Our approach differs from
97 recent studies in that our aim is to infer detailed cooling rate information about individual lava
98 flows and relate these to the observed columnar jointing patterns, rather than to infer global
99 mechanisms from an ensemble of observations from a wide range of field localities with
100 differing emplacement conditions. Our results and observations are complementary to recent
101 studies (e.g. Goehring and Morris 2008) and provide a unique dataset for further interpretative
102 studies.
103
104 The paper is set out as follows. In section two, the theoretical background to lava flow cooling is
105 summarised, and the time-dependence of cooling under different mechanisms is identified. In
106 section three, the geological mapping of the island of Staffa and the characteristics of the primary
107 flow units are described; the methodology for the measurement of columnar jointing patterns and
108 petrological analysis of the Staffa lava flows is presented in section four. In section five,
109 corresponding observations and results are presented, with analysis of jointing patterns and
110 calculation of cooling rate described in section six. In sections seven and eight, the implications
111 of the observations and their theoretical interpretation, for mechanisms of formation of columnar
112 jointing patterns, is discussed. Conclusions follow in section nine.
113
114
115

2. THE RELATIONSHIP BETWEEN ISOTHERM PROPAGATION AND COOLING MECHANISM IN A BASALT LAYER

Previous numerical modelling studies have attempted to use the dimensions of basaltic columns (e.g. striae spacing and face widths) to constrain cooling mechanisms. Grossenbacher and McDuffie (1995) showed that a constant ratio of striae spacing to column face width is consistent with purely conductive cooling. More recently, Goehring and Morris (2008) showed that a constant striae spacing, which they observe a few metres below lava flow tops in the Columbia River Basalt, is consistent with a convective cooling regime controlled by water infiltration into the fracture network. The different cooling mechanisms are characterised by different time dependence of isotherm propagation through a lava flow, which can be obtained from one-dimensional models of cooling through a basalt layer. The previous studies have been tested by assuming that pattern ordering depends entirely on the thermal regime, but not with an independent measurement of cooling rate obtained petrologically. Here we use the crystal size distribution of groundmass plagioclase in the basalt to estimate the propagation rate of the solidus isotherm through Staffa lava flows, and compare this with predictions of cooling models that include the latent heat release due to crystallisation.

Following Goehring and Morris (2008), we first consider one-dimensional conductive cooling of a static lava layer from its top only, including the effects of the latent heat release due to crystallisation. This is the classical Stefan problem, which results in a governing equation of the following form,

$$\frac{L\sqrt{\pi}}{c(T_m - T_0)} = \frac{e^{-\lambda^2}}{\lambda \,\mathrm{erf}\, \lambda} \quad , \qquad (1)$$

where L is the latent heat of solidification of basalt (taken to be 400 kJ kg^{-1} in this study; Turcotte and Schubert 2002), c is the specific heat capacity of basalt (taken to be 1 kJ kg^{-1} K^{-1} in this study; Turcotte and Schubert 2002), T_m is the initial temperature of the lava flow, T_0 is the ambient temperature and λ is the normalised depth in the flow, defined as

$$\lambda = \frac{z}{2\sqrt{\kappa t}} \qquad (2)$$

where z is the depth below the flow surface, κ is the thermal diffusivity of basalt (taken to be 8 x 10^{-7} m^2 s^{-1} in this study; Watson, 1994) and t is time. Full details of the model formulation are given in Turcotte and Schubert (2002), section 4.18. This model can be solved to predict the vertical position of a given isotherm in the layer as a function of time, and in this study Equation (1) was solved using Newton's method (e.g. Press et al., 1992) which converges rapidly because the right hand side is a monotonic function of λ (Turcotte and Schubert, 2002).

It is also important to consider conductive cooling and solidification from the base of the flow, due to its emplacement onto cold underlying rock. Following Degraff et al (1989), we also solve the Stefan problem for cooling from above and below simultaneously, where the lower layer cooling is described by a solution of similar form to Equation 1. Cooling and solidification from the upper and lower boundaries simultaneously results in a three layer structure, with the molten lava layer in the centre providing an insulating boundary such that cooling in the upper layer is independent of cooling in the lower layer and *vice versa*, because the molten layer temperature remains constant until complete solidification has occurred (Degraff et al 1989). We can thus

predict the propagation of the solidus isotherm independently for each layer, and its propagation rate in the upper layer is independent of whether or not there is cooling from below. Stefan approaches have been shown to be in good agreement with measurements at lava lakes (e.g. Turcotte and Schubert 2002), confirming that the density changes due to solidification at the surface do not destabilise the cooling lava layer.

The second model we consider is appropriate for convective cooling, which is envisaged to occur as a result of vaporisation of water that has infiltrated into cracks in the lava flow that are initially formed by conductive cooling (Ryan and Sammis, 1981; Budkewitsch and Robin, 1994). By solving the advection-diffusion equation appropriate to this mechanism of cooling, and comparing with field measurements of striae spacing, Goehring and Morris (2008) show that convective cooling can be characterised by a constant value of the Peclet number,

$$\mathrm{Pe} = \frac{vR}{\kappa}. \qquad (3)$$

where v is the solidus isotherm velocity and R is some representative length scale for the fracture pattern, taken to be the area-equivalent cylindrical radius to a hexagonal column of uniform side length. R was also observed to be constant in regions of convective cooling (Goehring and Morris 2008), so linear propagation of the solidus isotherm with time is consistent with a constant Peclet number. Field observations suggest that Pe = 0.3 ± 0.1 (Goehring and Morris, 2008), and in Fig. 2 we show the time-dependence of these model predictions for values of basalt properties appropriate for lava flows on Staffa (see also section six). In accordance with the form of equations (1) and (3), isotherm propagation which shows linear dependence on time is

consistent with convective cooling, and non-linear dependence is consistent with conductive cooling.

Figure 2 here

3. THE GEOLOGY OF STAFFA

The island of Staffa is situated off the west coast of the Isle of Mull, northwest Scotland (Fig. 3 inset). The island comprises ~30,000 m^2 with accessible shoreline exposure, and its geology is described by Bailey et al. (1925) and Keay and Keay (1994), with a 1:50,000 map based on the work of Bailey et al. (1925). The island is built from lava flow deposits that form part of the British Tertiary igneous province (Thompson 1982). As part of this study, we re-mapped the geology of the island; the resulting geological map is presented in Fig. 3.

Figure 3 here

The oldest unit outcropping on Staffa is a > 12 m thick basaltic pyroclastic deposit that we interpret to be an ignimbrite, that is exposed around the southern half of the island (Unit 1, Fig. 3). The ignimbrite comprises angular, sub-rounded juvenile scoria and spatter in a poorly sorted lapilli-tuff matrix. Clasts reach up to 1 m in diameter and some exhibit ropey surface textures and cowpat morphologies. Imbricated clasts indicate transport to the southwest. The ignimbrite exhibits a gross normal grading and the upper few metres are weakly stratified. This is overlain by a thick tholeiitic lava with well-developed columnar jointing and entablature zones (Unit 2,

208 Fig. 3), here called the Fingal's Cave lava flow. The flow is approximately 40 m thick at its
209 maximum (at Fingal's Cave) but thins northwards. Discontinuous lenses of rubbly breccia occur
210 along the base, overlain by coherent columnar-jointed lava, from 1 to >12 m thick, with a
211 vesicular base. This passes abruptly up into an entablature zone that can reach >10 m in
212 thickness and also thins northward. The entablature columns vary from well-formed, curvi-
213 columnar structures in the south to poorly-formed, hackly columns in the north. The lava exhibits
214 a well-defined upper crust, 2-4 m thick, comprising centimetre-thick bands of varying
215 vesicularity. The flow outcrops over much of the southern and northern parts of the island and
216 well-exposed sections occur in the cliffs around Staffa (e.g., Fingal's Cave and Am Buchaille,
217 Fig. 3).
218
219 In north-eastern parts of the island (e.g. Meallan Fulann, Fig. 3), Unit 1 is overlain by up to 15
220 cm of fine- to coarse-grained laminated sediments that may be volcanic ash, and then up to 8 m
221 of a unit that we interpret to be hyaloclastite (Unit 4; Fig. 3); at any rate there is evidence of
222 interaction with external water (see below). The hyaloclastite unit contains large coherent lobes
223 of solid lava up to a few metres thick that may be laterally extensive; large pods or blocks of lava
224 with radiating columns or hackly fractures, and irregular pillow structures indicating interaction
225 with external water (Fig. 4). The joints between pillows sometimes contain fine-grained
226 sediments; laminated sediments were also observed at the base of one of the lava lobes (Fig. 4).
227 The unit is dominated by a rubbly, hackly fractured matrix of small lava fragments, occasionally
228 with sediment filling cracks. One large lobe of coherent lava was sampled for crystal size
229 distribution analysis (see section 4.3).
230

231 Unit 4 is overlain by a pinkish-weathered, basaltic lava comprising a vesicular base and a
232 columnar-jointed core up to 7 m thick, in which joints are spaced 50-100 cm apart; a poorly-
233 developed upper crust is present at some locations. The youngest unit outcropping on the island
234 (Unit 6, Fig. 3) is a poorly-exposed columnar-jointed lava visible at the top of cliffs in the
235 northeast of the island. The island is cut by several thin basalt intrusions.
236
237 *Figure 4 here*
238 Two sample traverses were collected through columnar and entablature basalt. The first profile
239 was taken through a lobe of lava within the hyaloclastite unit on the eastern coast of Staffa
240 (locality 10). The lobe is approximately 5 m thick and the traverse samples the lower colonnade
241 (LC), entablature (ETB) and upper colonnade (UC), and is oriented approximately perpendicular
242 to the contacts between the different jointing zones. The second profile was collected in the
243 lower part of the main Fingal's Cave flow on the west coast of Staffa (locality 8), and samples
244 parts of the lower colonnade and entablature. The jointed basalts were difficult to sample, and
245 most samples were from edges or corners of jointed columns. We note that there could be
246 textural differences between the centres and margins of columns (e.g. Mattson et al. 2011).
247
248
249 **4. METHODOLOGY**
250
251 **4.1 Measurement of columnar jointing patterns**
252 At each locality (see Fig. 3), we measured the number of column sides, N, number of
253 neighbouring columns, column side length, L, internal angle between each side, θ, and maximum

diameter for each column, D (Figs. 1c and 5). The measurements were made in the field and from digital photographs which were taken vertically above each column top (with a scale bar), with a related sketch for each outcrop (Fig. 6). Where the long axes of columns were exposed, measurements of striae spacing, S, and column side lengths were also obtained to the nearest cm, using a tape measure. The precision of this measurement is conservative, because there was some variation of the striae spacing along the faces of the Staffa columns. A total of 702 column top areas were photographed and measured over eight localities, while >2000 striae spacings and 550 side lengths were measured on 26 columns at three localities.

Figure 5 here

Figure 6 here

Columnar jointing patterns were analysed using two key non-dimensional measures of pattern order. An assessment of pattern maturity was obtained from the Hexagonality Index, χ_N, (Budkewitsch and Robin 1994),

$$\chi_N = \sqrt{(f_5 + f_7) + 4(f_4 + f_8) + 9(f_3 + f_9) + 16 f_{10} + \ldots} \quad , \qquad (4)$$

where f_N is the fraction of column tops with N sides. A hexagonality index of zero represents perfectly ordered, hexagonal columns, while $\chi_N = 1$ indicates columns which are all 5- and/or 7-sided and $\chi_N = 2$ indicates columns that are all 4- and/or 8-sided. The degree of regularity of the jointing pattern was also estimated, as in previous studies (e.g. Goehring and Morris 2008) by the

277 relative standard deviation of column side angles, $\sigma(\theta)/\langle\theta\rangle$ (e.g. standard deviation of column
278 side angles divided by the mean side angle). A high relative standard deviation indicates
279 irregular column shapes with a wide variation of internal angles. In contrast, a low (near-zero)
280 value indicates a very regular set of columns. The relative standard deviations of the column top
281 areas ($\sigma(A)/\langle A\rangle$) and side length, ($\sigma(L)/\langle L\rangle$) were also investigated.
282
283 **4.2. Crystal Size Distributions**
284 Crystal size distributions (CSDs) are now routinely measured in studies of igneous rocks in order
285 to obtain information about the timescales of crystallisation. CSD theory has been described by
286 several authors (e.g. Cashman and Marsh 1988; Cashman 1990; Marsh 1998; Higgins 2002).
287 Processes of stereological correction for converting 2D crystal measurements to true 3D
288 measurements have been developed by Peterson (1996) and Higgins (1994; 2000). The key
289 principle is that, for batch crystallisation of a volcanic rock (which is appropriate for the Staffa
290 case) with crystal population density $n(L)$, where L is grain size, a plot of $\ln(n)$ vs L will
291 normally generate a straight line (the CSD), with gradient $-1/G\tau$ and intercept n_0, where G is the
292 mean growth rate, τ is the residence time of the crystals in the system and n_0 is the nucleation
293 density. This log-linear relationship probably arises because of an exponential increase in
294 nucleation rate with time, with simultaneous steady crystal growth (Marsh 1998). Thus by
295 assuming a value of G, the typical residence time of crystals can be obtained. Because the
296 parameter n_0 is defined per unit volume of magma, a stereological correction must be applied to
297 any 2D measurements of crystal size prior to calculations of the population density.
298

The two sample traverses were analysed for plagioclase crystal size distributions, with the aim of determining cooling rates for the natural columnar structures. Back-scattered electron images were taken from a polished thin section of each sample. Individual crystals were outlined by hand using the image analysis software package ImageJ (Rasband 1997-2009). The 2D area and Feret length (maximum possible length) were measured, along with the major and minor axes and the orientation of the ellipse best fitting the grain outline. Measurements were calibrated using the scale bar in the SEM image. Approximately 1200-1500 individual grains were measured for each thin section, except for STA10, where only ~430 grains were measured because of weathering. Only whole crystals were measured; crystals only partly in the image were not included in an attempt to minimise edge effects. A few grains that were clearly phenocrysts (having oscillatory or other internal zonation as well as very large crystal size) were ignored, as were some weathered patches, and where possible the total area measured was also corrected for this. Crystals with a Feret length below ~15 μm could not be measured accurately using this technique. To convert the crystal sizes and numbers to 3D populations, the program CSDCorrections 1.3 (Higgins, 2000) was used, assuming negligible preferred orientation. This is reasonable given that values of sample circular variance are ≥ 0.94 for all samples. Crystal shapes were estimated from the mode of intersection length, intersection width and intersection width/length ratios (Higgins 1994). A shape of 1: 4: 12 was used for the hyaloclastite traverse (locality 10), compared with 1: 3: 9 for the West Coast traverse (locality 8). The data were plotted as ln(n) *vs* size, where n is the 3D population density, using 4-5 logarithmic size intervals per decade (following Higgins 2000).

4.3. Analytical Methods

Back-scattered electron (BSE) images for textural observation and crystal size distribution analysis were taken using a JEOL-JSM-820 scanning electron microscope (SEM) at the University of Cambridge. Representative mineral compositions were obtained using a Cameca 5-spectrometer SX-100 electron microprobe, also at the University of Cambridge. A 2 μm, 15 kV, 10 nA beam was used to analyse major elements, with a 100 nA beam for minor elements (typically K, Cr, Ti and Mn).

5. RESULTS

5.1. Jointing Patterns in Staffa Columnar Basalt

Striae spacings measured on Staffa range from 2-15 cm, with a few wider striae of ~20-25 cm. At any given column, there was a high standard deviation of striae spacings, equivalent to ~30-50% of the average. Average striae spacings were equivalent within these uncertainties for the localities measured. No systematic variation of striae spacing with height in the flow was apparent, although because of the distribution of outcrops, striae spacing and column side lengths could only be measured in restricted parts of the flow. Height in the flow was measured relative to the flow base or entablature boundary. Column side lengths vary widely, from 28-101 cm, with two measurements at 145 cm (from locality 5). As with the striae spacing, there is no consistent systematic variation of column side length with height in the flow. At any given locality, the side lengths of individual columns can remain constant with height. Occasionally, step changes in side length of a given column are observed at column terminations. The average

striae spacing measured for each column is proportional to the average face width (Fig. 7); striae spacings are 7-20% of the face width at Staffa. This is consistent with observations from the Columbia River basalt and other similar flows, and corroborates the findings of previous studies (Degraff and Aydin 1987; Grossenbacher and McDuffie 1995; Goehring and Morris 2008) in suggesting underlying control by the mechanical properties of the rock (Young's Modulus and Poisson's ratio).

Figure 7 here

Column side lengths and column top areas are significantly smaller in the entablature compared with the colonnade (table 1). For example, in the entablature at locality 7, the average side length is only 12 cm, in comparison with 40 cm in the colonnade at locality 2. The transition between entablature and colonnade is typically sharp. At locality 4 the average side length in the colonnade is 36 cm. This decreases abruptly to 12 cm in the entablature, over a height of only 2 metres. At locality 4, average side lengths and column top areas were measured as a function of distance above the colonnade–entablature transition. Column side lengths show little variation with height over the observed range.

The maturity of columnar jointing patterns on Staffa was assessed using the hexagonality index (χ_N) and the relative standard deviation of column geometry as measures of order. For the colonnade localities χ_N is low, 0.79 – 0.87 (with one locality at 0.93), with <N> of 5.7-6.1, reflecting mature joint patterns dominated by 5-, 6- and 7-sided columns (Table 1; Fig. 8). The dominant column shape is 6-sided. The two entablature localities have differing hexagonality

368 index values. Locality 4 has a low χ_N of 0.82 and <N> of 5.9, similar to that of the colonnade
369 localities. Locality 7 has a higher χ_N of 1.20 with <N> of 5.3, indicating a crack pattern
370 containing abundant 4-, 5-, 6- and 7-sided columns, and dominated by 5-sided columns (table 1).
371 The lava lobe within the hyaloclastite unit at locality 10 also gave a high χ_N value of 1.11 with
372 <N> of 5.5 (Table 1). For comparison, joint patterns at the Giant's Causeway, Northern Ireland
373 give χ_N of 0.78 and 0.80 (Beard 1959; data from O'Reilly, 1879), very similar to that for Staffa.
374 Other datasets for jointed basalt give χ_N 0.92 and 1.06 (Devil's Postpile, California and Mount
375 Rodeix, Auvergne respectively; Beard 1959).
376
377 *Figure 8 here*
378
379 *Table 1 here*
380
381 The relative standard deviation of internal angles, $\sigma(\theta)/\langle\theta\rangle$, is low for all localities (Fig. 8).
382 Hexagonality correlates positively with $\sigma(\theta)/\langle\theta\rangle$, which is unsurprising because columns with
383 more sides must have a higher average internal angle, since the sum of the external angles of a
384 polygon is 360°. Thus patterns that have high hexagonality index (i.e. a higher relative
385 abundance of 3-, 4-, 5-, 7- and 8-sided columns) will have a greater spread of internal angles.
386 The colonnade localities give $\sigma(\theta)/\langle\theta\rangle$ of 0.15 – 0.19, indicating a relatively low spread of
387 column angles around the mean. The entablature localities have slightly higher $\sigma(\theta)/\langle\theta\rangle$ of 0.16
388 (locality 4) and 0.23 (locality 7), indicating a slightly wider spread of angles, at least for locality
389 7. For comparison, the Giant's Causeway has $\sigma(\theta)/\langle\theta\rangle = 0.13$, slightly lower than the Staffa
390 colonnade localities.

There is little difference in relative standard deviation of column side length, (σ(L)/<L>), between the colonnade and entablature samples. All localities gave similar values, 0.42 – 0.52 (Table 1; Fig. 8). However, the relative standard deviation of column top area, σ(A)/<A>, shows a clear contrast between facies, reflecting the general decrease in column dimensions in the entablature. Hexagonality index correlates positively with both σ(A)/<A>, which results from the tendency for columns with more sides to have a greater maximum diameter, and <A> (e.g. Rivier and Lissowski 1982). The colonnade localities have low σ(A)/<A>, 0.35 – 0.58, whereas the entablature localities give higher values of 0.57 (locality 7) and 0.66 (locality 4). These data indicate that entablature columns are slightly more variable in shape and size, as well as being smaller than those of the colonnade. The Giant's Causeway data give σ(A)/<A> = 0.34, again slightly lower than the Staffa colonnade samples (Fig. 8).

Average values for the lava lobe within the hyaloclastite unit are similar to those from the entablature (Table 1; Fig. 8). Although relatively few column dimensions could be measured, and no striae were observed, average side length is clearly greater in the upper and lower colonnade structures, and smaller in the central entablature zone.

5.2. Crystal Size Distributions

Two sample profiles were analysed: a profile through part of the Fingal's Cave lava colonnade at locality 8, and a profile through the lava lobe at locality 10 (Fig. 3). The West Coast (Fingal's Cave) samples typically show a linear CSD, with a down-turn at crystal lengths below ~ 100 μm (true crystal size), which equates to a measured Feret length of < 40 μm. This is probably related

414 both to difficulty in measuring the smallest grains, and a true deficiency of crystals in the
415 smallest size ranges due to growth. Fits to the straight parts of the CSDs are very good, with R^2 >
416 0.995. The gradient is similar throughout the Lower Colonnade, but lower for the entablature
417 (Fig. 9). As the gradient is equivalent to $1/G\tau$ this suggests either a longer crystallisation time (τ)
418 or higher growth rate (G) for the entablature. The intercept is also slightly higher in the
419 entablature.
420
421 *Figure 9*
422
423 The samples from the lava lobe within the hyaloclastite unit also show linear CSDs (Fig. 9), with
424 a sharp down-turn at lengths below ~60 μm (true crystal size, or < 25 μm Feret diameter). Fits to
425 the straight parts of the CSD are again very good, with R^2 > 0.993. There is no systematic
426 difference in gradient or intercept between the samples in this traverse. Gradients are in the range
427 -0.0238 μm^{-1} to -0.0191 μm^{-1} (Table 2).
428
429 *Table 2 here*
430
431 **5.3. Sample Petrology**
432 Several of the samples show signs of alteration, which mainly affects olivine and glass. The
433 basalts contain sparse phenocrysts of plagioclase + clinopyroxene + olivine (typically altered),
434 with a coarse-grained groundmass of randomly oriented, tabular plagioclase, clusters of granular
435 pyroxene, olivine, and oxides of varying morphology. Clinopyroxene phenocrysts commonly

436 contain lath-shaped inclusions of plagioclase in their cores. Plagioclase, clinopyroxene and
437 olivine crystals show strong compositional zoning at their margins.
438
439 In the samples from the lava lobe within the hyaloclastite unit, planar-sided patches of
440 groundmass between plagioclase grains are extensive and show evidence of silicate liquid
441 immiscibility in the form of quenched droplets of dark, probably Fe-rich material (Fig. 10). No
442 analyses could be obtained owing to the small size of the droplets; however they are interpreted
443 as Fe-rich and Si-rich droplets on the basis of previous studies (e.g. Roedder and Weiblen 1970;
444 Philpotts, 1979; Jakobsen et al. 2005; Charlier and Grove 2012). The droplets appear to be most
445 fine-grained in the entablature section of this unit.
446
447 *Figure 10 here*
448
449 The morphology of the oxides grains varies both within and between the traverses. In the thin
450 lava lobe within the hyaloclastite unit, all the oxides are cruciform to dendritic (Fig. 10);
451 however the oxides in samples from the entablature are finer and more delicate in structure than
452 those in the columnar sections. In the West Coast traverse, oxides are tabular and subophitic in
453 lower (columnar) parts (e.g. STA7). They become less tabular, more elongate, and even hopper-
454 shaped with height (e.g. STA9), while the entablature contains dendritic forms (STA10).
455
456
457
458 **5.4. Mineral Compositions**

459 Groundmass plagioclase has calcic cores (An_{73}-An_{89}) with overgrowth rims that are strongly and
460 progressively zoned to oligoclase-anorthoclase. The plagioclase contains up to 1.41 wt% FeO,
461 0.35 wt% MgO and 0.18 wt% TiO_2 (Fig. 11). Kinks in minor element concentrations with
462 decreasing X_{An} probably indicate fractionation of olivine ± pyroxenes followed by Fe-Ti oxides
463 (Fig. 11), and thus confirm that plagioclase was crystallising throughout the cooling time of the
464 lava flow. Clinopyroxene is augitic, with Mg# 80-57. Core and rim compositions of
465 clinopyroxenes overlap, but the rims extend to more evolved compositions with lower Mg#,
466 lower Cr_2O_3, higher TiO_2 and higher Na_2O. Opaque minerals are mainly ilmenite and
467 titanomagnetite. The titanomagnetite has variable TiO_2 content (65-95 mol% Usp), suggesting
468 crystallisation over a wide range of temperatures and/or a range of fO_2 conditions. Temperature
469 estimates were obtained from coexisting ilmenite-titanomagnetite pairs in the Fingal's Cave lava,
470 with oxide formulae calculated according to Stormer (1983), and using QUILF (Andersen et al.
471 1993). These gave temperatures of 968-1007 °C and log fO_2 -10.8 to -11.6 (0.0 to 0.2 log units
472 above the FMQ buffer).
473
474 *Figure 11 here*
475
476 **6. ANALYSIS**
477
478 **6.1. Use of Crystal Size Distributions to Constrain Cooling Rates for Staffa Basalts**
479 Our approach is essentially to assume that plagioclase crystallisation occurs throughout the
480 liquidus-solidus temperature interval, and to estimate the residence time for plagioclase using
481 CSDs, to give an average cooling rate over that interval. In detail, we assume that the lava is

482 emplaced at its liquidus, which is estimated to be ~1145 to 1190°C, based on MELTS estimates
483 (Ghiorso and Sack 1995) using bulk compositions of Staffa Magma Type lavas given by
484 Thompson et al. (1986). This range of liquidus temperatures is also consistent with
485 experimentally-determined liquidus temperatures for the Rattlesnake Hill basalt (1150-1180°C,
486 Philpotts 1979) which shares many of the textural and chemical features of the Fingal's Cave
487 lava. The solidus temperature is approximately 950°C, based on experimental observations
488 (Philpotts 1979). Thus the crystallisation interval is approximately 200-240°C, and we assume
489 that plagioclase crystallises throughout this interval. Plagioclase phenocrysts are essentially
490 absent, indicating that plagioclase did not start to grow before emplacement of the flow. The
491 residence time for plagioclase, obtained using CSDs, therefore gives us the time for the lava flow
492 to cool between 1170°C and 950°C. We recognise that this simplification could include some
493 cooling time while the flow was being emplaced, but we consider this to be small relative to the
494 total cooling time. By determining this cooling time for different sampling positions through the
495 lava, the propagation of the 950°C isotherm can be tracked. We recognise that there may be
496 textural differences in crystal size distribution between the margins and centres of basaltic
497 columns (Mattson et al. 2011) but we were not able to control for this in our sampling, except
498 that column cores were not sampled. However, all our sample profiles were collected in the same
499 way, and the uncertainties associated with the sampling are probably small relative to
500 uncertainties in crystal growth rates, for example.

501

502 In order to use the CSD to estimate the solidus isotherm propagation for a particular sampling
503 position, an estimate of the crystal growth rate is required, which is unconstrained by the sample
504 properties (see section 3.3). However, estimates of plagioclase growth rates in basaltic dykes and

505 flows have been reasonably well constrained in previous petrological studies. These estimates
506 range from 1.3×10^{-6} mm/s for dykes 30-50 cm thick (Ikeda 1977, reported in Cashman 1990) to
507 1.3×10^{-9} to 9.0×10^{-9} mm/s for dykes 15-30 m thick (Ikeda 1977; Kneedler 1989; reported in
508 Cashman 1990). In comparison, crystallisation rates for surface lavas range from 1×10^{-9} to $6 \times$
509 10^{-10} mm/s (Makaopuhi lava lake, Cashman and Marsh 1988) and 2×10^{-6} to 4×10^{-9} mm/s
510 (Mauna Loa, Cashman 1990), to 1.7×10^{-7} to 1.3×10^{-8} mm/s for Kilauea lavas (Burkhard 2002).
511 We therefore assumed growth rates of 10^{-8} to 10^{-9} mm/s as most representative of the likely
512 crystallisation conditions. Fig. 12 shows isotherm propagation trends for crystal growth rates of
513 10^{-9} and 10^{-8} mm s^{-1}, for the Fingal's Cave lava flow sample traverse at locality 8, where this
514 flow has a thickness of about 12 m.
515
516 *Figure 10 here*
517
518 Fig. 12 suggests that the 950°C isotherm propagates linearly with time through the interior of the
519 flow (within the range of sample positions). The cooling time to 950 °C for the flow interior,
520 calculated using G = 10^{-9} mm s^{-1}, has a comparable magnitude to previous estimates and
521 observations of basalt cooling times (e.g. Cashman 1990; Turcotte and Schubert 2002) which
522 suggest times of 12-20 months at depths of about 8 metres below the flow top. However, the
523 isotherm propagation time trend should reach zero time at the upper margin of the flow. If we
524 use the higher crystal growth rate (10^{-8} mm s^{-1}) we calculate isotherm propagation times that are
525 much shorter (indicating much more rapid cooling) for the flow interior, which is inconsistent
526 with previous observations as outlined above. This reveals a clear inconsistency in our use of the
527 same value of *G* near the flow margin, because the isotherm propagation time trend for the flow

528 interior cannot be extrapolated to match cooling conditions in the flow margin (Fig. 12). The
529 only reasonable conclusion is that crystal growth rates are significantly higher near the flow
530 margin compared to the interior. The effect of this would be to change the gradient of the
531 isotherm propagation time in this region; much closer sampling would be required to test this
532 hypothesis.

533

534 Irrespective of the details of the cooling trends near the flow margin, our data clearly show a
535 linear isotherm propagation rate with depth in the flow (Fig. 12). We cannot fit the alternative
536 curved trend (cf Fig. 2) to the data for any reasonable physical conditions (temperature contrasts,
537 latent and specific heats of basalt). From our comparison of field measurements of the solidus
538 isotherm propagation with one-dimensional cooling models (Fig. 2), we therefore infer that
539 convective cooling is the dominant mechanism for the Fingal's Cave lava at locality 8, combined
540 with strong conductive cooling at the flow top itself. We found the ratio of striae spacing to face
541 width to be in accord with measurements at other basalt flows (Goehring and Morris 2008), and
542 found little variation in their absolute values within the colonnades sampled, within the
543 uncertainty of our measurements. Constant striae spacing has been shown to be consistent with
544 convective cooling of the basalt due to the presence of water within fractures (Goehring and
545 Morris 2008) and therefore supports our interpretations based on isotherm propagation rates.
546 This result for Staffa is consistent with those of Goehring and Morris (2008) for the Columbia
547 River Basalt flows, which also suggest a convective cooling mechanism within the interior of the
548 flow.

549

550 **7. EVOLUTION AND MATURITY OF NATURAL JOINTING PATTERNS**

551 We have used the hexagonality index, χ_N, as a measure of the maturity of a jointing pattern,
552 following Budkewitsch and Robin (1994). The most mature patterns show relatively low values
553 of χ_N, including those in the Fingal's cave colonnade (Fig. 8; table 1) and at Giant's Causeway
554 (Beard 1959); the most mature jointing patterns are commonly agreed to have formed in the most
555 slowly cooled lavas. However, the apparent strong variations in growth rate at the flow top
556 (inferred above) raise a key question. These jointing patterns must have been initiated under very
557 rapid cooling conditions: how do they achieve their very mature flow centres? Gray et al. (1976)
558 argued that such mature patterns (with Y-shaped crack terminations, i.e. internal angles
559 approaching 120°) could not nucleate by simple fracturing in a plane, but must result from
560 maturation of an initial joint pattern, by selective propagation of certain joint orientations.
561 Pattern coarsening is therefore achieved by termination of certain joints and rearrangement of the
562 neighbouring columns (Budkewitsch and Robin 1994; Jagla 2004; Goehring and Morris 2005).
563
564 Jagla (2004) carried out numerical simulations of jointing patterns for a range of stages in the
565 temporal evolution of a contracting elastic sheet. Evolution of the crack pattern occurred
566 spontaneously in order to reduce the mechanical energy of the pattern (Jagla 2004). We digitised
567 the resulting patterns (Jagla 2004, Fig. 2b-d) and the data show a positive correlation between
568 $\sigma(A)/\langle A \rangle$ and χ_N, with the more mature patterns giving lower χ_N (Fig. 8). In the numerical
569 simulations pattern maturation occurred by increasing the regularity of polygon cross-sections by
570 crack termination and merging smaller columns with fewer sides (Jagla 2004), resulting in
571 decreased χ_N and decreased column area variability ($\sigma(A)/\langle A \rangle$). The basalt joint patterns
572 measured on Staffa approach the most mature numerical pattern (Fig. 8), but although the use of
573 several localities exposed through erosion has given a spread of statistical data, it is clearly

574 difficult to image serial sections through the joint patterns in a lava flow. We therefore suggest
575 that the initial jointing pattern at the flow top on Staffa may have been similar to those observed
576 at lava lakes, where the hot lava surface is in contact with air (or water). This is supported by
577 data from lava lakes, digitized from Peck and Minakami (1968), which give high χ_N (0.77-1.0),
578 low numbers of sides <N> and high column area variability (σ(A)/<A>, table 1, Fig. 8). Overall,
579 the average number of column faces, <N>, also increases as χ_N decreases for basalt. We suggest
580 that an initial jointing pattern with similar statistical variability to the lava lakes nucleated at the
581 surface of the Staffa flow and propagated downward, rapidly become more mature by selective
582 joint termination and merging of adjacent columns.
583
584 Hexagonality can also vary independently of <N> or relative standard deviations of column
585 dimensions. Fig. 8 also shows different mature statistical distributions of 2D polygons, including
586 one based on a Poisson distribution (Crain 1978), and two close packing arrangements developed
587 for division of territory within bird species (Tanemura and Hasegawa 1980). In all three the
588 average number of column sides is 6.00 (Budkewitsch and Robin 1994). The Poisson distribution
589 has χ_N = 1.33, while the random close packing model has χ_N = 0.80 and the regular close packing
590 model χ_N = 0.54 (Fig. 8). The basalt columns show similar χ_N to these mature theoretical
591 distributions (Fig. 8), with slightly higher χ_N for the entablature, consistent with a higher cooling
592 rate and less mature jointing pattern. However, the basaltic jointing patterns overlap most closely
593 with the theoretical random close packing arrangement (Fig. 8). In previous models of joint
594 propagation (e.g. Ryan and Sammis 1981; Degraff and Aydin 1993; Lachenbruch 1962), lateral
595 joint spacing (*i.e.* column diameter) is controlled by the distance over which tensile stress can be
596 relieved by the formation of a new *stria*. Wider joint segments relieve stress over a greater area,

leading to increased joint spacing. The 'hard centres' of the random close-packed circles are therefore analogous to the regions over which tensile stress is relieved by cracking and thus may have some physical meaning for the thermal joint patterns. Hexagonality index will decrease to zero for a perfectly regular hexagonal arrangement of columns, but the smallest value observed for the Fingal's Cave lava is approximately 0.80, indicating that even the most regular basaltic columns have some inherent variability (Goehring and Morris 2008).

8. ORIGIN OF ENTABLATURE AND COLONNADE STRUCTURES ON STAFFA

The origin of basaltic entablature has previously been ascribed to flooding of the flow surface with water (Saemundsson 1970; Long and Wood 1986), interaction between propagating joint sets (Xu 1980; Spry 1962) and to intrinsic discontinuities in pattern scaling (Goehring and Morris 2005). The occurrences of columnar jointing on Staffa probably reflect more than one mode of entablature formation. For example, the lava lobe at locality 10 shows clear upper and lower columnar layers, while the centre of the lobe is an irregular, hackly entablature (see Fig. 4). The average side length of the columns decreases smoothly upward into the entablature, and can be seen to increase across the entablature-upper colonnade boundary. There is no clear textural difference between entablature and colonnade samples from the lava lobe in the hyaloclastite unit, and their CSDs are equivalent. This indicates no strong change in cooling rate at the entablature, and suggests that the entablature represents an interaction between two converging joint sets.

In contrast, the Fingal's Cave lava has no upper colonnade exposed, but a very thick entablature (several metres at Fingal's Cave itself) which thins northward. Column dimensions in the colonnade are consistent across the flow. At Fingal's Cave there is an abrupt change in lengthscale and pattern maturity at the colonnade – entablature boundary, accompanied by a clear change in rock texture to finer grainsize and dendritic oxides. This suggests rapid quenching, probably by ingress of surface water into the joints (Long and Wood 1986; Lyle 2000). This is supported by the cooling rate calculations presented in this study, which indicate convective cooling (see earlier). On the north coast of Staffa, the Fingal's Cave flow is much thinner, as is the entablature, which grades upwards into an upper colonnade. Furthermore, while the entablature at Fingal's Cave is strongly curvi-columnar with clearly continuous columns, on the north coast the columns are less well-defined. Separating the two localities is a sizeable exposure of hyaloclastite breccia that outcrops in the northeast of the island (see Fig. 3). We therefore suggest that part of the Fingal's Cave flow was emplaced into a lake or similar feature, resulting in surface flooding and water ingress along joints, and hence the rapidly quenched entablature in the south of the island. The northern parts of the flow were probably not erupted into water; the entablature here may reflect the interaction of propagating joint sets from the upper and lower colonnade. Thus entablature jointing can form through different mechanisms, even within a single flow.

9. CONCLUSIONS

We have studied columnar jointing in basaltic lava flows on the island of Staffa, using a combination of field mapping and measurement of column dimensions, sample petrology and

642 plagioclase crystal size distributions (CSDs) coupled with theoretical constraints to identify the
643 dominant cooling mechanism. The main conclusions from this study are as follows:
644 1. There are four different lava flow units on the island of Staffa, which provide a range of
645 exposure of columnar jointing at both column tops and column sides. Basaltic colonnades consist
646 of dominantly 5, 6 and 7-sided columns, with a hexagonality index value very similar to that of
647 Giant's Causeway and other basaltic columnar jointed localities.
648 2. There is no systematic variation of striae spacing or column face width within the colonnades,
649 which is consistent with observations at other field areas, and has been previously interpreted as
650 consistent with convective cooling of the interior of the lava flow by water.
651 3. The column side lengths and top areas are significantly smaller in the lava flow entablature
652 compared with the colonnades. Two entablature localities studied in detail show widely different
653 values of hexagonality index, one similar to the colonnade values and the other indicating
654 abundant 4, 5, 6, 7 -sided columns, with similar hexagonality index values to a nearby
655 hyaloclastite lava flow unit.
656 4. The hexagonality index provides a useful measure of maturity (i.e. tendency of columns to be
657 six-sided) for natural columnar jointing patterns. Trends in hexagonality index are consistent
658 with those of other commonly-used measures such as relative standard deviation of column top
659 area, face width and internal angle.
660 5. The initial jointing pattern that formed on the flow surface at Staffa was probably immature,
661 with high χ_N and variable column dimensions, perhaps similar to the patterns observed at lava
662 lakes. As the jointing pattern propagated down into the flow interior, it matured by selective joint
663 termination and merging of columns. The mature pattern has similar statistical variability to a
664 random close packing of hard spheres.

6. Crystal size distributions from samples at different heights within one colonnade were used to infer the propagation of the solidus isotherm. When compared with the predictions of one-dimensional theoretical models, this suggested that the isotherm propagation was consistent with a convective cooling mechanism within the colonnade interior, supporting the lack of systematic variation in striae spacing or face width. Conductive cooling models cannot fit the isotherm propagation data. A distinctly different cooling mechanism must have operated close to the margin, which is inconsistent with convective cooling for any range of Peclet numbers that are considered reasonable for basaltic lava flows.

7. Sample petrology and CSD measurements suggest that the entablature can form from both the interaction of propagating joint sets and from flooding of the flow surface by water, and the most widely exposed unit on Staffa shows evidence of both mechanisms operating on the same flow.

8. Crystal size distributions, coupled with one-dimensional numerical models, can provide a useful tool for field interpretation of lava flow cooling mechanisms, but more work is needed to find robust independent methods for determining crystal growth rates.

ACKNOWLEDGEMENTS

We gratefully acknowledge a grant from the Edinburgh Geological Society which contributed towards fieldwork costs. We thank Chiara Petrone for assistance with electron microprobe analyses, Bob Mehew for helpful discussions and photographs, Thierry Menand for useful discussions about fracturing, and Scottish Natural Heritage for permission to work on the island. MCSH was supported by a Junior Research Fellowship from Trinity College, Cambridge.

REFERENCES

Andersen DJ, Lindsley DH, Davidson PM (1993) QUILF: A Pascal program to assess equilibria among Fe-Mg-Ti oxides, pyroxenes, olivine and quartz. Computers and Geosciences 19:1333-1350

Bailey EB, Anderson EM, Burnett GA, Richey JE, Lee GW, Wright WB, Wilson GV, Thomas HH (1925) The geology of Staffa, Iona and western Mull. *Memoirs of the Geological Survey of Scotland*

Beard CN (1959) Quantitative study of columnar jointing. Geological Survey of America Bulletin 70:379-382

Budkewitsch P, Robin P-Y (1994) Modelling the evolution of columnar joints. Journal of Volcanology and Geothermal Research 59:219-239

Burkhard DJM (2002) Kinetics of crystallization: example of micro-crystallization in basalt lava. Contributions to Mineralogy and Petrology 142:724-737

Cashman KV (1990) Textural constraints on the kinetics of crystallization of igneous rocks. Reviews in Mineralogy 24:259-314

Cashman KV, Marsh BD (1988) Crystal size distribution (CSD) in rocks and the kinetics and dynamics of crystallization II: Makaopuhi lava lake.

Charlier B, Grove TL (2012) Experiments on liquid immiscibility along tholeiitic liquid lines of descent. Contributions to Mineralogy and Petrology (in press), doi: 10.1007/s00410-012-0723-y

Crain IK (1978) The Monte-Carlo generation of random polygons. Computers and Geosciences 4:131-141

Degraff JM, Aydin AA (1987) Surface morphology of columnar joints and its significance to mechanics and direction of joint growth. Geological Society of America Bulletin 99: 605-617

711 Degraff JM, Aydin AA (1993) Effect of thermal regime on growth increment and spacing of
712 contraction joints in basaltic lava. Journal of Geophysical Research 98: 6411-6430
713 Degraff JM, Long PE, Aydin AA (1989) Use of joint-growth directions and rock textures to infer
714 thermal regimes during solidification of basaltic lava flows. Journal of Volcanology and
715 Geothermal Research 38:309-324
716 Ghiorso MS, Sack RO (1995) Chemical mass transfer in magmatic processes. IV. A revised and
717 internally consistent thermodynamic model for the interpolation and extrapolation of liquid-solid
718 equilibria in magmatic systems at elevated temperatures and pressures. Contributions to
719 Mineralogy and Petrology 119:197-212
720 Goehring L, Morris SW (2005) Order and disorder in columnar joints. Europhysics Letters
721 69:739-745
722 Goehring L, Morris SW (2008) Scaling of columnar joints in basalt. Journal of Geophysical
723 Research 113:B10203
724 Gray NH, Anderson JB, Devine JD, Kwasnik JM (1976) Topological properties of random crack
725 networks. Mathematical Geology 8:617-626
726 Grossenbacher KA, McDuffie SM (1995) Conductive cooling of lava: columnar joint diameter
727 and stria width as functions of cooling rate and thermal gradient. Journal of Volcanology and
728 Geothermal Research 69:95-103
729 Higgins MD (1994) Numerical modelling of crystal shapes in thin sections: Estimation of crystal
730 habit and true size. American Mineralogist 79:113-119
731 Higgins MD (2000) Measurements of crystal size distributions. American Mineralogist 85:1105-
732 1116
733 Jagla EA (2004) Maturation of crack patterns. Physical Review E 69:056212

734 Jakobsen JK, Veksler IV, Tegner C, Brooks CK (2005) Immiscible iron- and silica-rich melts in
735 basalt petrogenesis documented in the Skaergaard intrusion. Geology 33:885-888
736 Keay J, Keay J (1994) Collins Encyclopaedia of Scotland. Harper Collins Publishers, London
737 Lachenbruch AH (1962) Mechanics of thermal contraction cracks and ice-wedge polygons in
738 permafrost. *Special Paper of the Geological Society of America* **70**, 69pp
739 Long PE, Wood BJ (1986) Structures, textures and cooling histories of Columbia River basalt
740 flows. Geological Society of America Bulletin 97:1144-1155
741 Lyle P (2000) The eruption environment of multi-tiered columnar basalt lava flows. Journal of
742 the Geological Society, London 157:715-722
743 Marsh BD (1998) On the interpretation of crystal size distributions in magmatic systems. Journal
744 of Petrology 39:553-599
745 Mattson HB, Caricchi L, Almqvist BSG, Caddick MJ, Bosshard SA, Hetenyi G, Hirt A.M.
746 (2011) Melt migration in basalt columns driven by crystallization-induced pressure gradients.
747 Nature Communications 2:299 doi: 10.1038/ncomms1298
748 Müller G (1998a) Experimental simulation of basalt columns. Journal of Volcanology and
749 Geothermal Research 86:93-96
750 Müller G (1998b) Starch columns: Analog model for basalt columns. Journal of Geophysical
751 Research 103:15239-15253
752 O'Reilly JP (1879) Explanatory notes and discussion on the nature of the prismatic forms of a
753 group of columnar basalts, Giant's Causeway. Transactions of the Royal Irish Academy 26:641-
754 728
755 Peck DL, Minakami T (1968) The formation of columnar joints in the upper part of Kilauean
756 lava lakes, Hawaii. Geological Society of America Bulletin 79:1151-1116

757 Peterson TD (1996) A refined technique for measuring crystal size distributions in thin section.
758 Contributions to Mineralogy and Petrology 124: 395-405
759 Philpotts AR (1979) Silicate liquid immiscibility in tholeiitic basalts. Journal of Petrology 20:99-
760 118
761 Press WH, Flannery BP, Teukolsky SA, Vetterling WT (1992) Numerical Recipes. Cambridge
762 University Press
763 Rasband WS (1997-2009) ImageJ. U.S. National Institutes of Health, Bethesda, MD.
764 http://rsb.info.nih.gov/ij. Accessed 28 June 2008
765 Rieter M, Barroll MW, Minier J, Clarkson G (1987) Thermo-mechanical model for incremental
766 fracturing in lava flows. Tectonophysics 142:241-262
767 Rivier N, Lissowski A (1982) On the correlation between sizes and shapes of cells in epithelial
768 mosaics. Journal of Physics A: Mathematical and General 15: L143-L148
769 Roedder E, Weiblen PW (1970) Silicate liquid immiscibility in lunar magmas, evidenced by melt
770 inclusions in lunar rocks. Science 167:641-644
771 Ryan MP, Sammis CG (1981) The glass transition in basalt. Journal of Geophysical Research
772 86:9519-9535
773 Saemundsson K (1970) Interglacial lava flows in the lowlands of southern Iceland and the
774 problem of two-tiered columnar jointing. Jokull 20:62-77
775 Spry A (1962) The origin of columnar jointing, particularly in basalt flows. Australian Journal of
776 Earth Sciences 8:191-216
777 Stormer JC (1983) The effects of recalculation on estimates of temperature and oxygen fugacity
778 from analyses of multi-component iron-titanium oxides. American Mineralogist 66:586-594

779 Swanson DA (1967) Yakima basalt of the Tieton River area, south central Washington.
780 Geological Survey of America Bulletin 78:1077-1110
781 Tanemura M, Hasegawa M (1980) Geometrical models of territory. 1. Models for synchronous
782 and asynchronous settlement of territories. Journal of Theoretical Biology 82:477-496
783 Thompson RN (1982) Magmatism of the British Tertiary Volcanic Province. Scottish Journal of
784 Geology 18:49-107
785 Thompson RN, Morrison MA, Dickin AP, Gibson IL, Harmon RS (1986) Two contrasting styles
786 of interaction between basic magmas and continental crust in the British Tertiary Volcanic
787 Province. Journal of Geophysical Research 91:5985-5997
788 Tomkeieff SI (1940) The basalt lavas of the Giant's Causeway district of Northern Ireland.
789 Bulletin of Volcanology 6:89-143
790 Turcotte DL, Schubert G (2002) Geodynamics. 2nd Ed. Cambridge University Press
791 Watson EB (1994) Diffusion in volatile-bearing magmas in Carroll, M.R. & Holloway, J.R. (eds)
792 Volatiles in Magmas. Min. Soc. Am. Rev. Min. 30:371-411
793 Weinberger R (1999) Initiation and growth of cracks during desiccation of stratified muddy
794 sediments. Journal of Structural Geology 21:379-386
795 Xu S (1980) Discussion on the morphological charactersistics of two-layer columnar joints in
796 basalt and their forming mechanism. Geological Review (in Chinese, with English abstract),
797 26:510-515
798
799
800
801

FIGURE AND TABLE CAPTIONS

Fig. 1

Schematic columnar jointing architecture. (a) and (b) Possible relationships between entablature and colonnade; (c) Measurable dimensions of an individual column include the diameter (D), side length (L), striae spacing or width (S) and the internal angles (θ).

Fig. 2

Theoretical predictions of the time to cool to 950^{o}C for a 10 m thick basalt layer initially emplaced at 1170^{o}C. The solid lines show the case of conductive cooling and solidification (Stefan solutions), and the dashed lines show the case of convective cooling due to vapourisation of water for Peclet numbers of 0.3 (dashed line) and 0.4 (dotted line). Convective cooling is consistent with propagation of the solidus isotherm that is linear with time.

Fig. 3

Geological map (right) and stratigraphic section (left) for Staffa. Inset shows location of the Isle of Mull (shaded) with arrow to indicate the location of the island of Staffa. Localities studied are marked with large dots and a locality number (small dots indicate topographic spot heights).

Fig. 4

Field relationships within Unit 4, interpreted as hyaloclastite. (a) Lobe of lava (right) with well-developed columns (colonnade, C) at base and hackly entablature (ETB) in upper part (upper colonnade not seen in this view). The lava is underlain by bedded sediments (S) of variable

grainsize. Lava pod with radiating cracks is seen to upper left on the far side of a steeply dipping fault. (b) Pillow-like structures in the same unit; narrow bands of sediment separate some pillows (arrowed). (c) Cherty sediment between pillow structures.

Fig. 5

Field examples of jointing from Staffa. (a) The Fingal's Cave flow at its thickest point showing upper entablature, lower colonnade and underlying ignimbrite; (b) Typical column faces with sub-horizontal *striae*; (c) View of column tops in the entablature, Staffa, showing 4- to 6-sided, polygonal columns.

Fig. 6

Examples of typical entablature (top, locality 7) and colonnade (bottom, locality 1) flow tops measured for statistical parameters. Each increment on the scale bar represents 10 cm.

Fig. 7

Width of joint increments (striae widths, S) follows a rough proportionality with column side lengths (L) for Staffa (black diamonds), in agreement with previously published data from other column jointed basalt localities (Boiling Pots, Hawaii, Ryan and Sammis 1978; First Watchung, New Jersey, USA, Ryan and Sammis 1978; Prehistoric Makaopuhi lavas, Hawaii, Ryan and Sammis 1978; and Columbia River basalts, USA (Grossenbacher and McDuffie 1995; Goehring and Morris 2008). Contours represent lines of constant S/L.

Fig. 8

Column top measurements from experimental and natural jointing patterns. Hexagonality index (χ_N) *vs* (a) average number of sides, <N>; (b) relative standard deviation of column side lengths, σ(L)/<L>; (c) relative standard deviation of column top areas, σ(A)/<A>; (d) relative standard deviation of column internal angles, σ(θ)/< θ >. Red squares: entablature and hyaloclastite (H) jointing patterns from Staffa. Triangles: measurements from other columnar jointed basalt localities, including Mount Rodeix (MR), Auvergne, Devil's Postpile (DP), California, and the Giant's Causeway (GC), Ireland. Data for MR and DP taken from Budkewitsch and Robin (1994); data for GC from Beard (1959) and digitised from O'Reilly (1879). Black dots: numerically simulated distributions from (1) Crain, 1978; (2) Random close packing model, Tanemura and Hasegawa, 1980, reported in Budkewtisch and Robin (1994); (3) Regular close packing model digitised from Tanemura and Hasegawa (1980). Un-numbered dots are progressively maturing patterns digitised from Jagla (2004); arrow indicates direction of increasing maturity. Large open circles: Lava lake jointing patterns digitised from Peck and Minakami (1968), for Makaopuhi lava lake (ML) and Alae lava lake (AL). Filled circles: columnar jointing in silicic ignimbrite; data from Wright et al. (2011). Crosses are desiccation crack patterns in starch (digitised from Mueller 1998).

Fig. 9

Crystal size distributions for the Fingal's Cave lava flow (A, top) and for the lava lobe within the hyaloclastite unit (B, bottom). Both sets of samples give CSDs that are linear with a down-turn at low crystal size. See text for details. Dashed lines indicate entablature samples.

Fig. 10

Silicate liquid immiscibility in the hyaloclastite lava lobe. Top: back-scattered SEM image showing bright Fe-rich droplets immersed in a silicic (mid-grey) liquid. Droplets coalesce and adhere to plagioclase crystal margins. Tabular, euhedral plagioclase (pl, dark grey); cruciform/ dendritic oxides (ox, white); pyroxene (px, grey). Scale bar 25 μm. Bottom: Plane-polarised photomicrograph showing liquid immiscibility between plagioclase grains (centre). Dendritic oxides (black) and altered olivine/ pyroxene (brown) can also be seen. Scale bar 50 μm.

Fig. 11

Minor element concentrations (TiO_2, FeO and MgO) in plagioclase from Staffa as a function of Anorthite content (X_{An}). All elements show a break in slope which probably corresponds to crystallisation of new phases (Fe-Ti oxides and clinopyroxene) during plagioclase crystallisation.

Fig.12

The time to cool from emplacement temperature (~1170 °C) to 950 °C, estimated from crystal size distributions for the Fingal's Cave lava, with assumed crystal growth rates of 10^{-9} mm s^{-1} (circles) and 10^{-8} mm s^{-1} (squares). The solid line is a linear regression fit with equation $y = 1.18x + 35.8$, and the dashed line shows the approximate position of the flow top.

Table 1

Statistical data from natural and experimental jointing patterns. Also shown are statistical data calculated from previously published data: [1] from images in O'Reilly (1879); [2] Beard 1959; [3] Budkewitsch and Robin (1994); [4] from images in Peck and Minakami (1968); [5] from data of Wright et al. (2011); [6] Crain (1978); [7] Tanemura and Hasegawa (1980), reported in Budkewitsch and Robin (1994); [8] from images in Jagla (2004); [9] from images in Mueller (1998)

Table 2

Crystal size distributions for samples from the Fingal's cave flow, west coast traverse (locality 8) and the hyaloclastite lava lobe (locality 10).

FIGURES AND TABLES

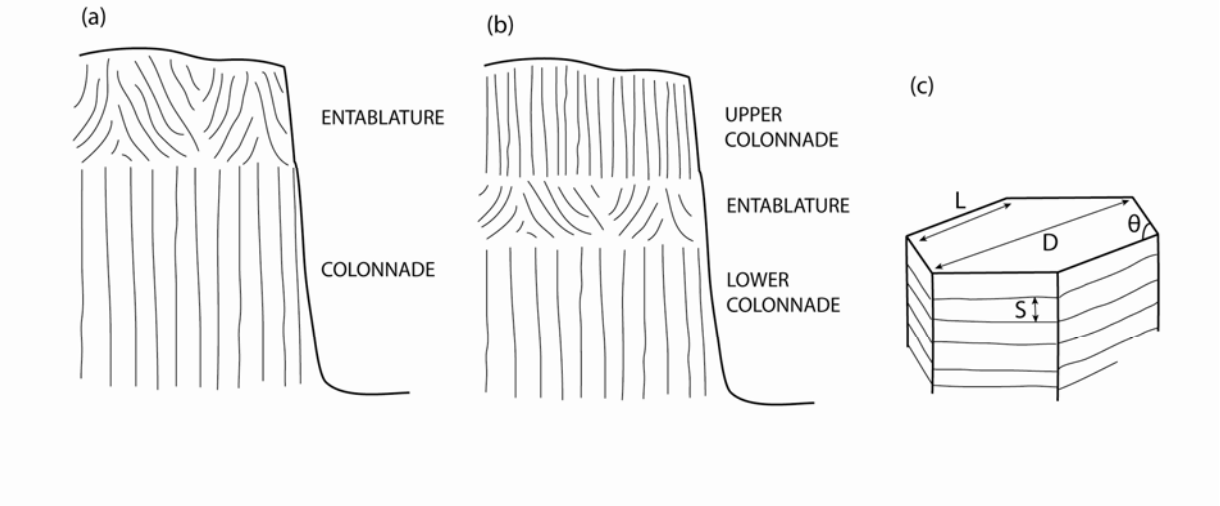

Figure 1

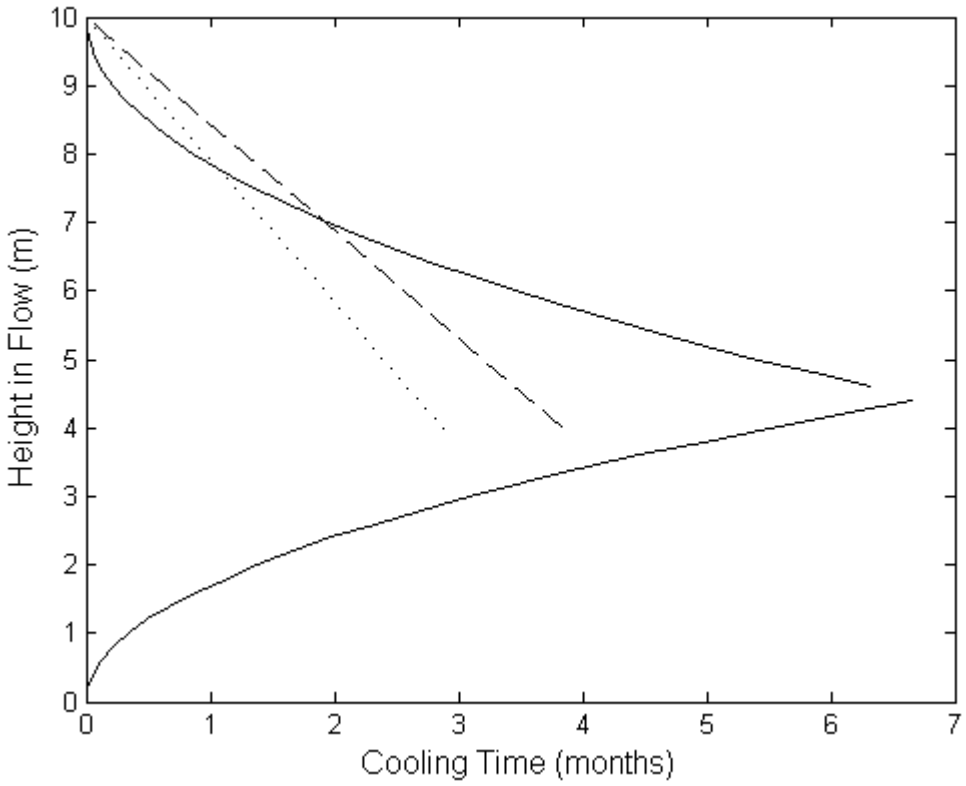

931

932

933 Figure 2

934

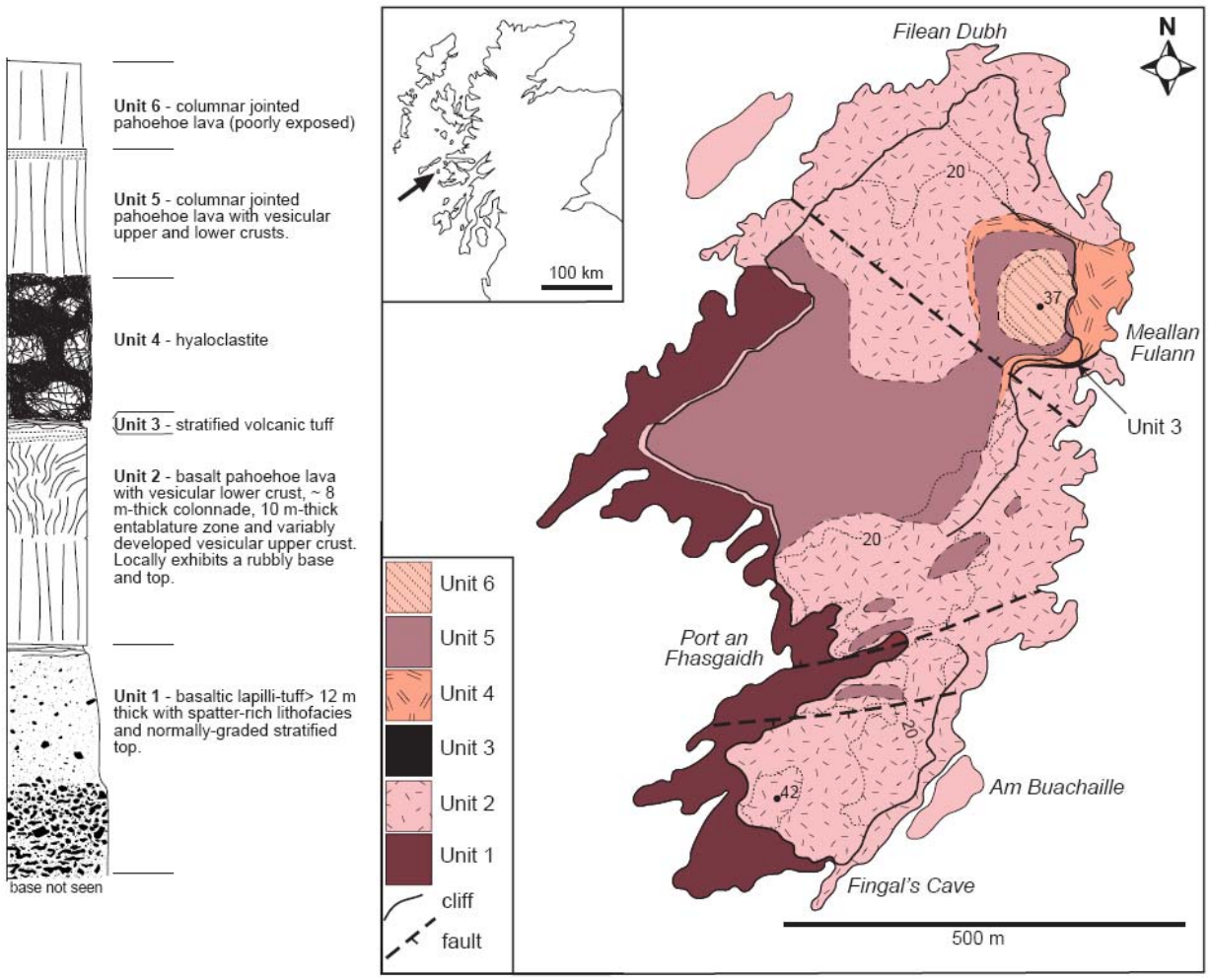

935

936 Figure 3

937

938

939

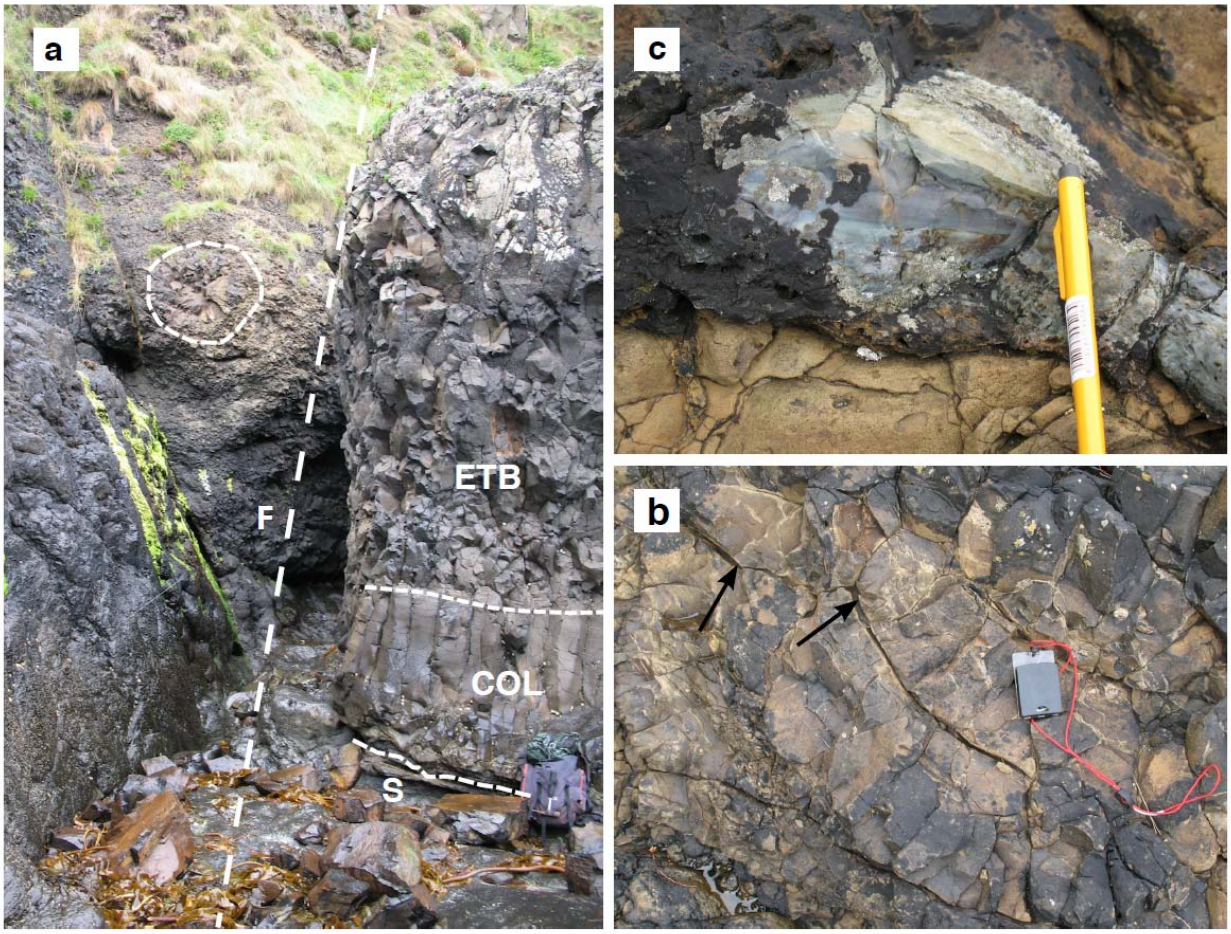

940

941 Figure 4

942

943

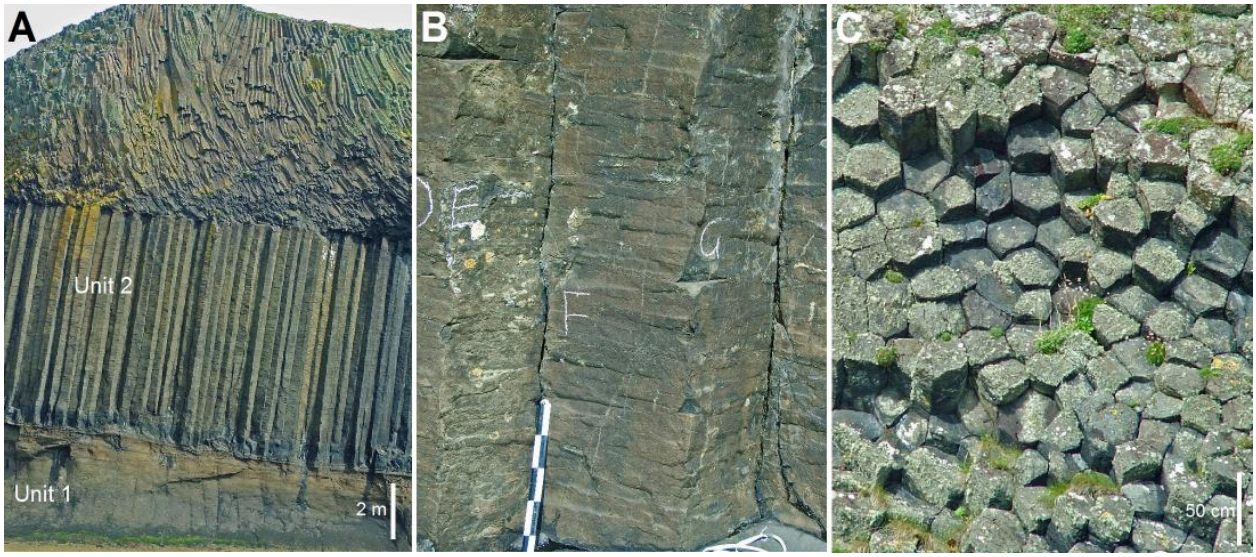

Figure 5

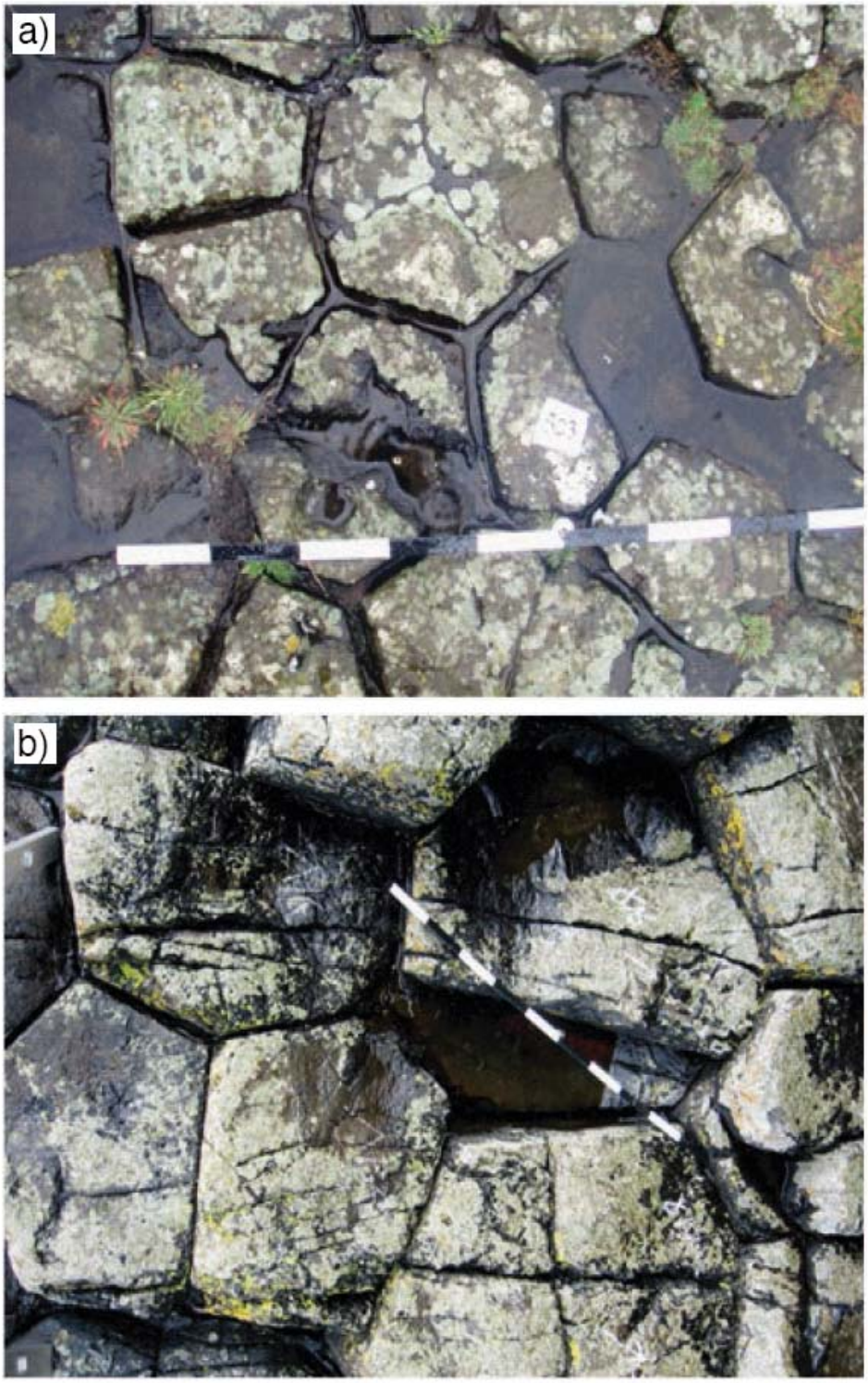

961

962

963 Figure 6

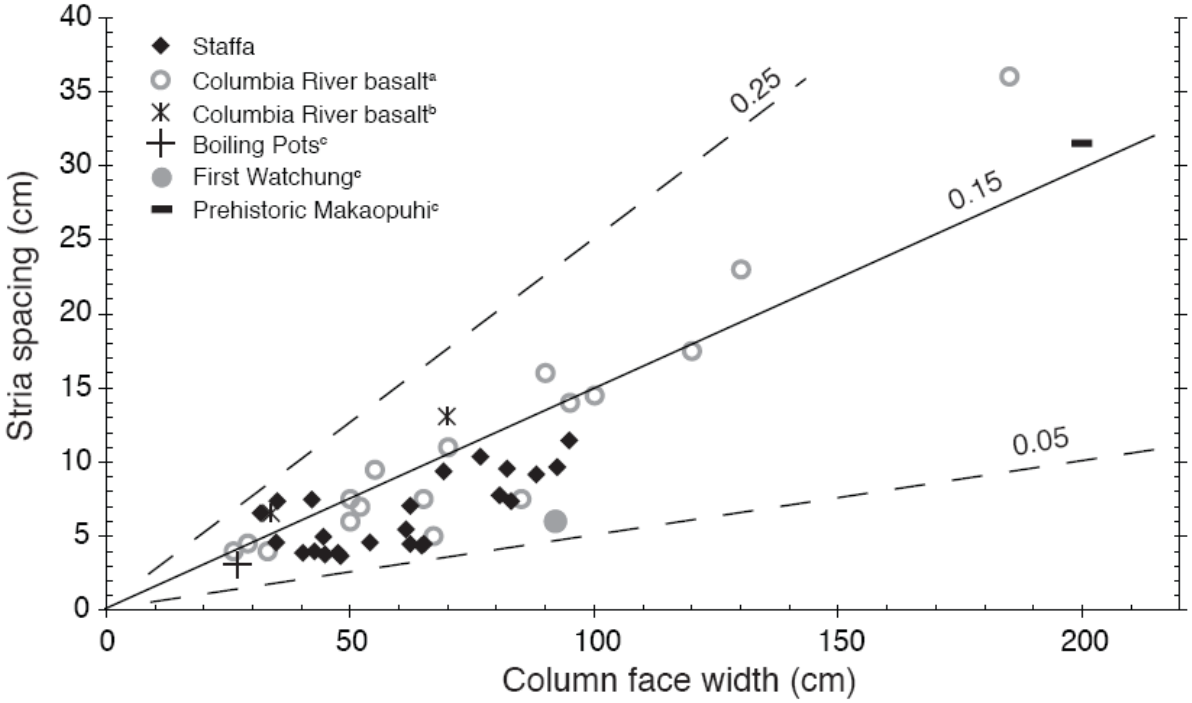

964

965 Figure 7

966

967

968

969

970

971

972

973

974

975

976

977

978

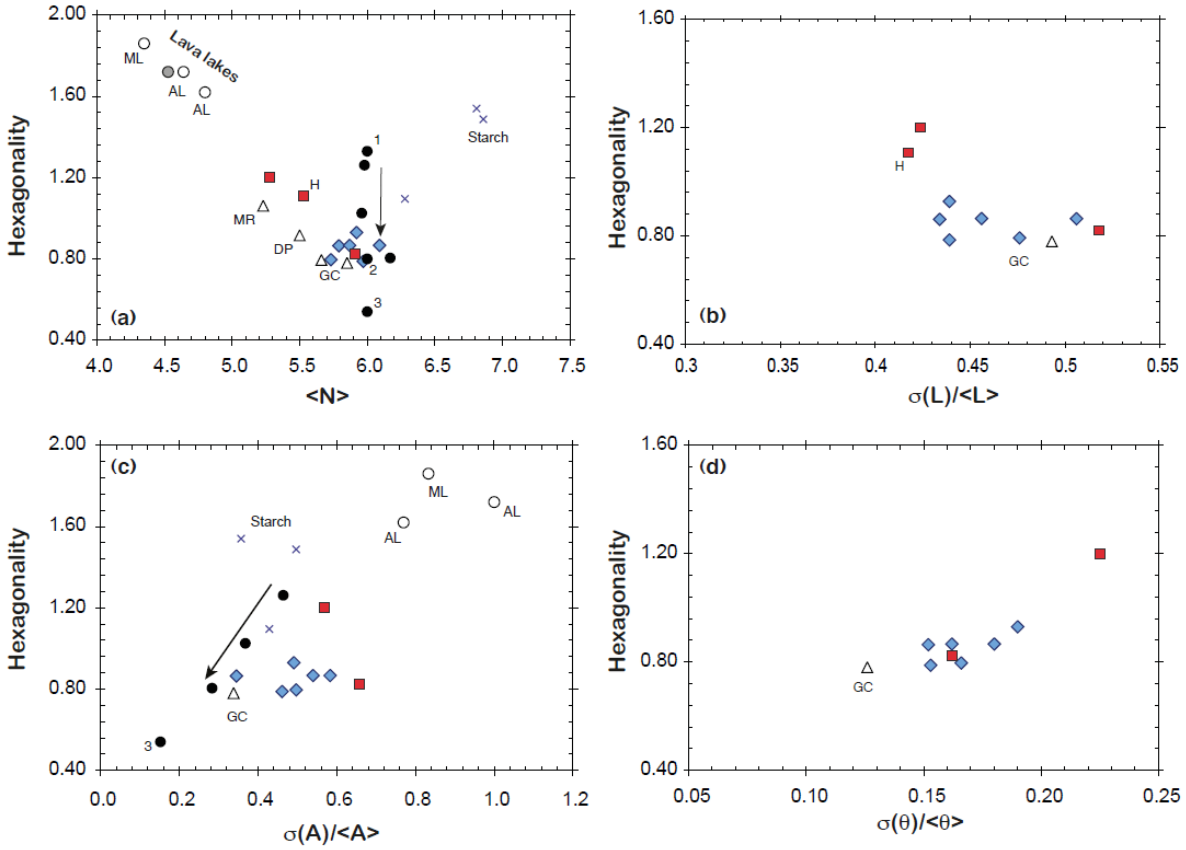

979

980 Figure 8

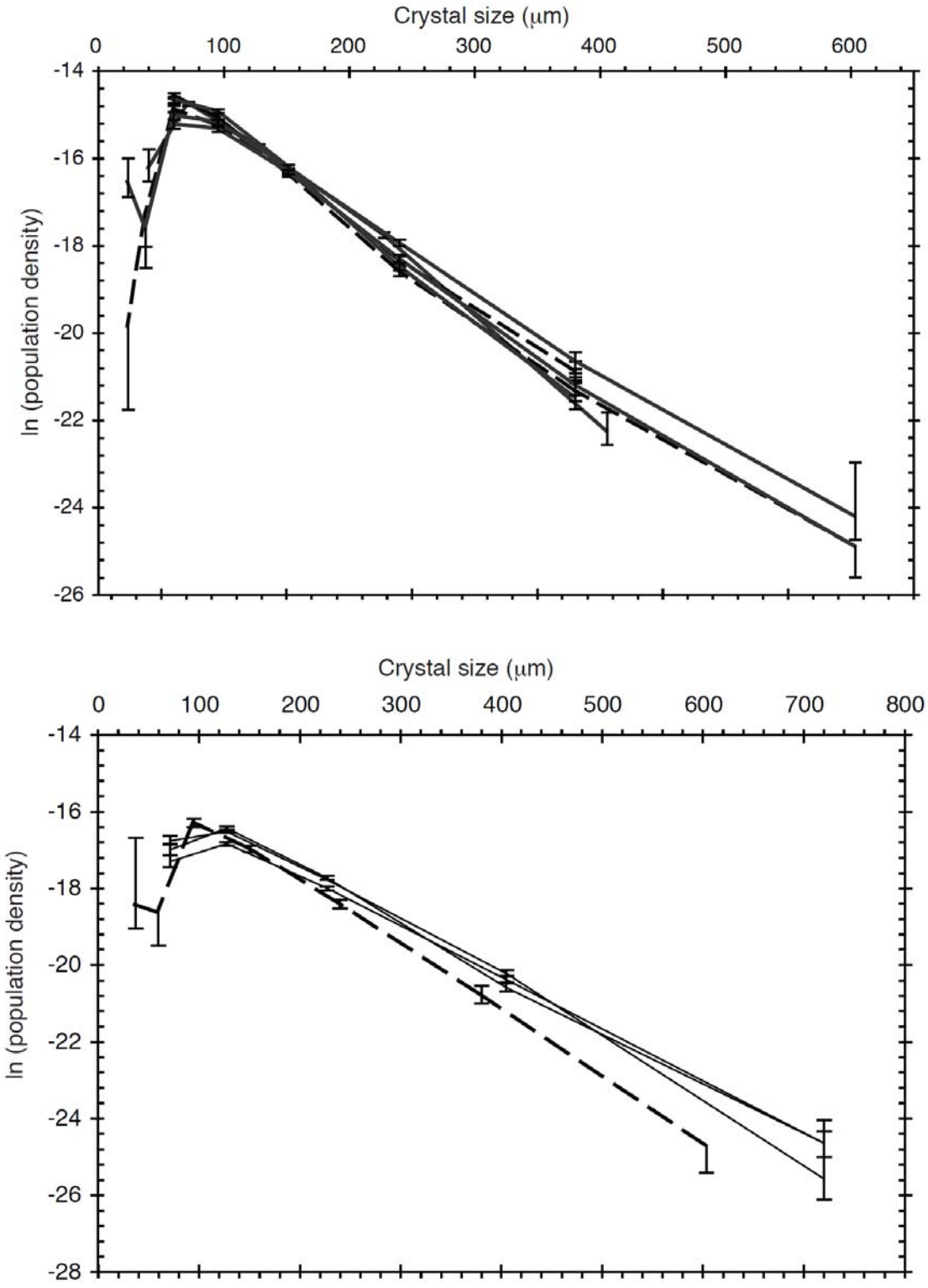

981

982 Figure 9

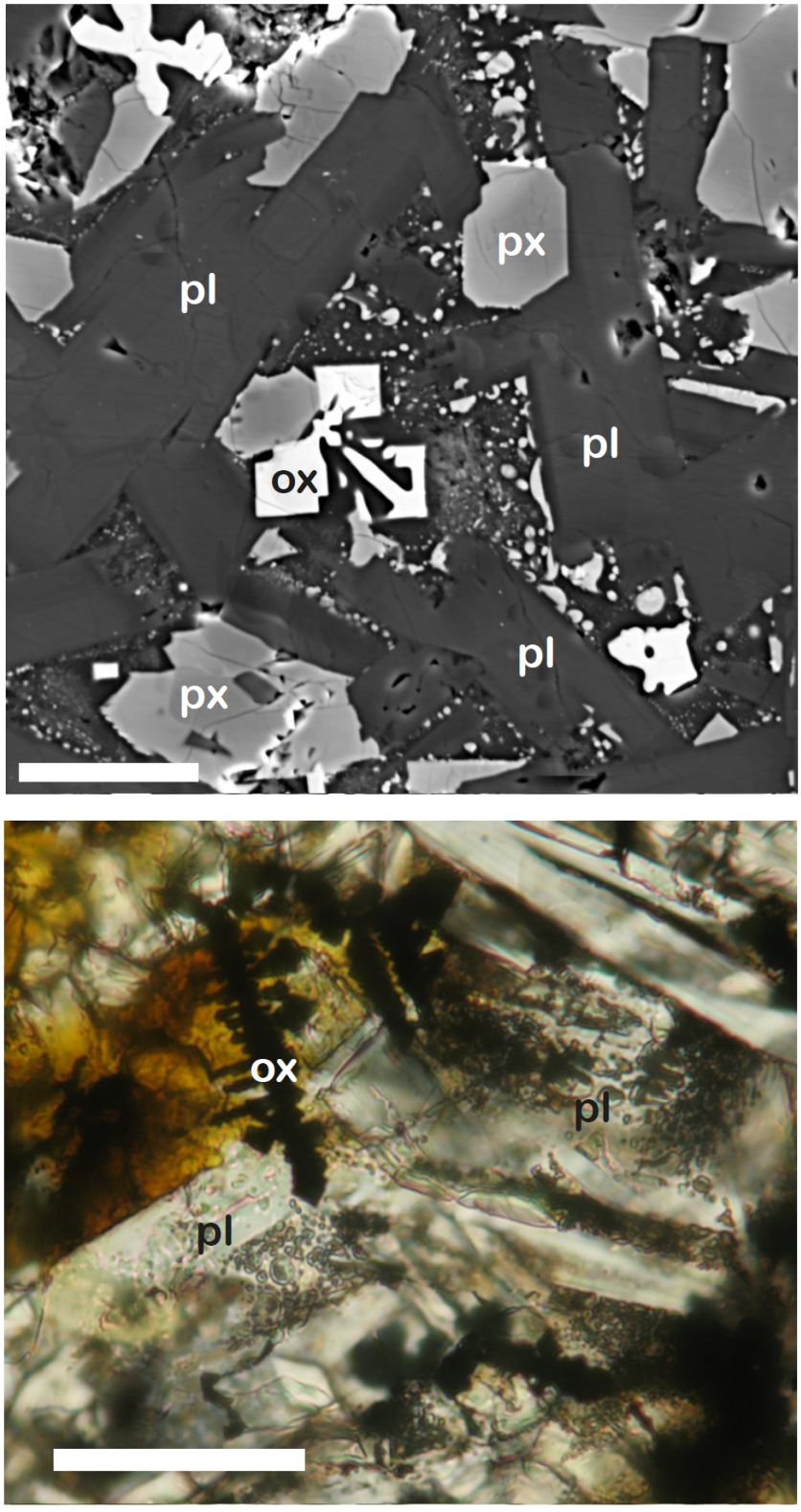

983

984 Figure 10

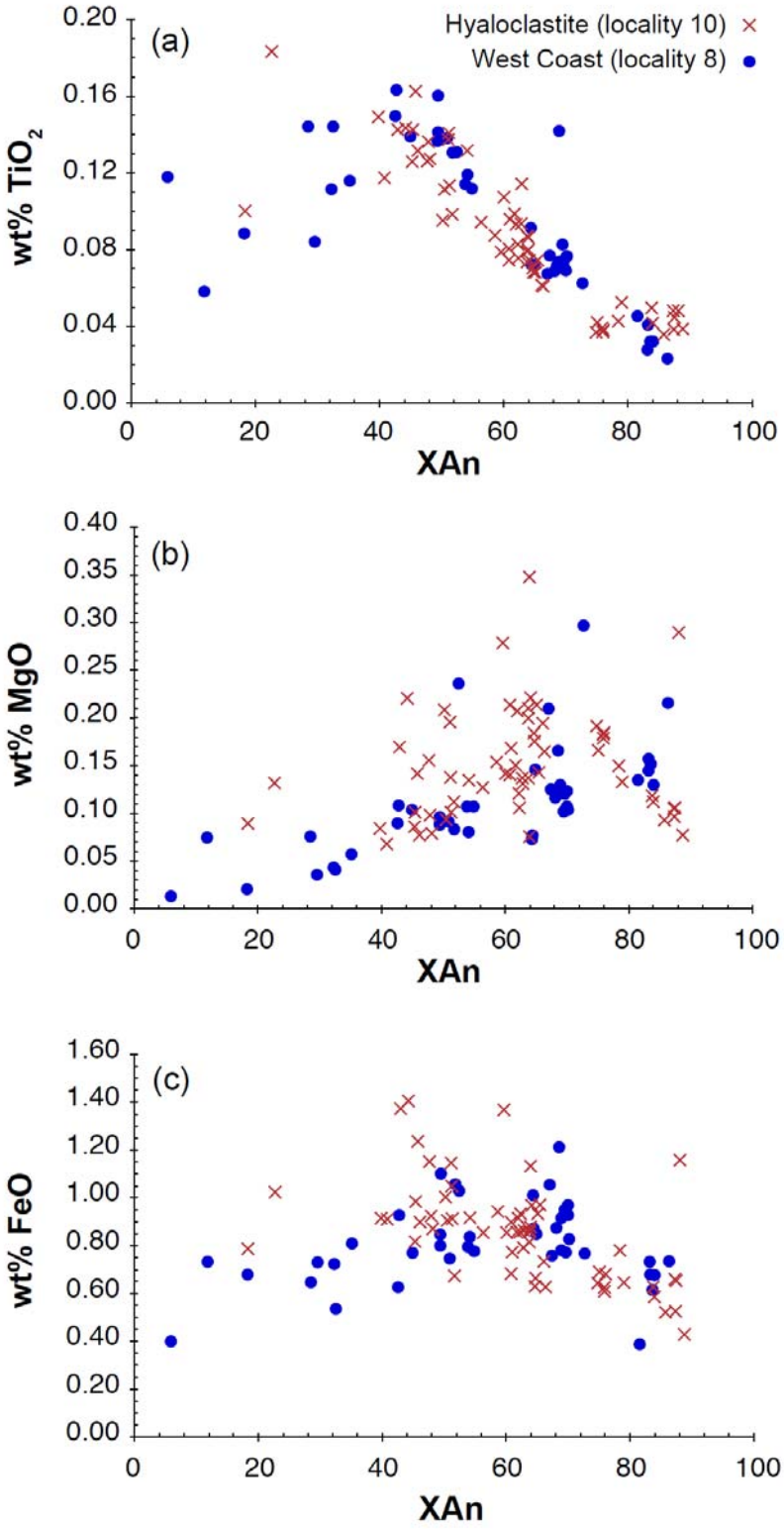

985

986 Figure 11

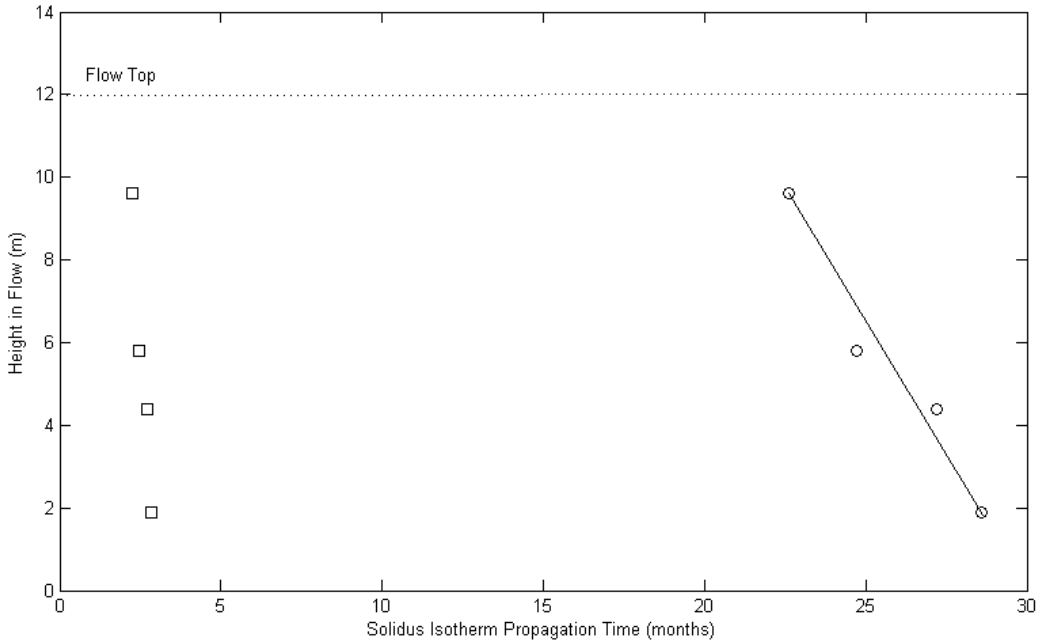
Flow Top
Height in Flow (m)
Solidus Isotherm Propagation Time (months)
0
2
4
6
8
10
12
14
0
5
10
15
20
25
30

Figure 2

	No. columns	Avg no. sides	χ_N	Mean column diameter (cm)	Mean side length <L> (cm)	σ(L)	σ(L)/<L>	column top area <A> (cm^2)	σ(A)	σ(A)/<A>	Mean internal angle °	σ(θ)	σ(θ)/<θ>
Locality 1 (colonnade)	71	5.7	0.80	77.5	38.3	18.2	0.476	3157	1571	0.497	117.8	19.5	0.166
Locality 2 (colonnade)	138	5.8	0.86	83.4	40.1	17.4	0.434	3709	1278	0.345	118.2	18	0.152
Locality 3 (colonnade)	53	5.9	0.93	91.8	41.8	18.3	0.439	4329	2124	0.491	118.9	22.6	0.190
Locality 5 (colonnade)	68	5.9	0.87	113.5	53.9	24.6	0.456	7520	4059	0.540	118.7	19.2	0.162
Locality 6 (colonnade)	100	6.1	0.87	74.6	33	16.7	0.506	2836	1654	0.583	120.7	21.8	0.180
Locality 8 (colonnade)	37	6.0	0.79	87.8	41.8	18.3	0.439	4326	1992	0.461	119.7	18.4	0.153
Locality 4 (entablature)	58	5.9	0.82	24.5	11.6	6.01	0.518	308.5	202.7	0.657	119.1	19.3	0.162
Locality 7 (entablature)	172	5.3	1.20	21.4	11.9	5.04	0.424	271.1	154.1	0.568	111.9	25.2	0.225
Locality 10 (hyaloclastite)	13	5.5	1.11		16.4	6.84	0.417						
Giant's Causeway [1]	76	5.9	0.78		27.7	13.7	0.493			0.338	119	13.7	0.126
Giant's Causeway [2]	400	5.7	0.80										
Devil's Postpile [3]	400	5.5	0.92										
Mount Rodeix, Auvergne [3]	200	5.2	1.06										
Alae lava lake [4]	26	4.8	1.62							0.77			
Alae lava lake [4]	72	4.6	1.72							1.0			
Makaopuhi lava lake [4]	55	4.4	1.86							0.833			
Paycuqui ignimbrite, Cerro Galan, Argentina [5]		4.5	1.72	75									
Poisson model [6]	46000	6.0	1.33										
Anti-clustered (random close-packing) model [7]	675	6.0	0.80										
Mature (regular close-packing) model [7]	500	6.0	0.54							0.152			
Numerical model, t = 10 [8]	110	6.0	1.26							0.464			
Numerical model, t = 20 [8]	99	6.0	1.03							0.368			
Numerical model, t = 280 [8]	93	6.2	0.80							0.283			
Starch, d = 7mm [9]	100	6.8	1.54							0.357			
Starch, d = 11mm [9]	100	6.3	1.10							0.429			
Starch, d = 19 mm [9]	100	6.9	1.49							0.497			

Table 1

	Locality 8				Locality 10					
	STA7	STA8	STA9	STA10	STA11	STA12	STA13	STA14	STA16	STA15
Facies	Lower colonnade	Lower colonnade	Lower colonnade	Entablature	Lower colonnade	Lower colonnade	Lower colonnade	Entablature	Entablature	Upper colonnade
Height above base (cm):	33	280	420	800	70	135	180	240	275	380
Total area measured (mm^2)	3.86	3.88	3.88	1.49	1.81	1.81	1.51	1.81	1.81	1.81
No. crystals measured	1114	1464	1465	431	1143	1396	1510	1278	1390	1464
CSD gradient = -1/Gt	-0.0133	-0.014	-0.0154	-0.0168	-0.0205	-0.0191	-0.0238	-0.0193	-0.0233	-0.0198
±	0.0002	0.0005	0.0007	0.0007	0.0006	0.0005	0.0006	0.0005	0.0006	0.0005
ln (population density)	-15.07	-14.70	-14.35	-14.53	-13.32	-13.35	-12.64	-13.5	-12.85	-13.26
±	0.08	0.07	0.07	0.14	0.1	0.08	0.09	0.07	0.09	0.07
Crystallisation rate (mm/s)	1.0E-09	1.0E-09	1.0E-09	1.0E-09	5.0E-08	5.0E-08	5.0E-08	5.0E-08	5.0E-08	5.0E-08
Residence time t (day)	870	827	752	689	11	12	10	12	10	11.7

Table 2